A refocusing modified velocity map imaging electron/ion spectrometer adapted to synchrotron radiation studies

Gustavo A. Garcia[a),b)] and Laurent Nahon[a),b),c)]
Laboratoire L.U.R.E., Bât 209D, Université de Paris Sud, 91898 Orsay Cedex, France

Chris J. Harding, Elisabeth A. Mikajlo, and Ivan Powis
School of Chemistry, University of Nottingham, NG7 2RD Nottingham, United Kingdom

We present a modified velocity map imaging (VMI) spectrometer to be used in angle-resolved molecular photoionization studies in the gas phase with synchrotron radiation (SR) in the VUV/soft x-ray range. The main modifications as compared to the original design of Eppink and Parker [A. T. J. B. Eppink and D. H. Parker, Rev. Sci. Instrum. **68**, 3477 (1997)] are an open repeller which allows the VMI spectrometer to be coupled to an independent dispersive electrostatic analyzer for combined operation in coincidence mode experiments, and the introduction of a coupled double Einzel lens in the flight tube in order to collect the full 4π solid angle for higher kinetic energy particles. The length and position of the lenses have been optimized by a genetic algorithm to obtain the maximum kinetic energy possible without compromising the energy resolution. Ray-tracing simulations and SR experiments show that the lenses can increase the kinetic energy bandwidth by a factor of up to 2.5. Furthermore, a remarkable improvement in the radial focusing of the particles' momenta can be achieved when the lens array is operated in optimum fashion. The accuracy in the determination of the angular parameters, already satisfactory in the original VMI design, is not compromised by the lens operation. Experimentally, we succeeded in collecting 4π electrons with 14 eV kinetic energy and 6% relative energy resolution with a detector of 36 mm effective diameter, despite the larger ionization volume given by the SR as compared to laser multiphoton experiments. We predict that, by changing to a detector diameter of 70 mm and reducing the focal length by a third, particles with energies up to 200 eV could be collected by applying 10 kV to the repeller electrode. © *2005 American Institute of Physics.* [DOI: 10.1063/1.1900646]

I. INTRODUCTION

Electron/ion imaging techniques provide multiplex capabilities that offer full vectorial information (both energy and 3D-angular distribution) about photon-induced fragmentations and chemical reaction dynamics and have, since their introduction[1] in the late 80's, become widely used tools in chemical physics.[2] Since then, the simple approach consisting of projecting the expanding sphere of charged particles onto a 2D position sensitive detector (PSD) with homogeneous fields[3] has been refined with the introduction by Eppink and Parker in 1997 of the velocity map imaging (VMI) technique.[4] In this enhanced mode a specific focusing effect is produced, owing to the lens effects created by hollow electrode structures, so that a charged particle's impact position onto the PSD depends only on the initial momentum of the particle and is independent, within certain limitations, of the exact point of creation in an ionization volume of finite extent. The transverse velocity component and angle of the particle's recoil are still mapped to the radial and angular coordinate in the recorded image, but the reduced sensitivity to precise initial position leads to a strong deblurring of the recorded images. For a given physical geometry the degree of focusing is dependent on the simple ratio of the potentials applied to the extractor and repeller electrodes (see Fig. 1), $\rho_{ext} = V_{ext}/V_{rep}$. Such a scheme has now been implemented in numerous experiments and, when an optimized value is selected for ρ_{ext}, provides kinetic energy resolutions, $\Delta E/E$, typically in the few percent range.[5]

VMI instrumentation has been designed and mostly used for laser studies of chemical dynamics in which the produced ions or electrons have typical kinetic energies of no more than a few eV. In the case of very low energies, a magnifying lens has been proposed and implemented into a VMI instrument by Offerhaus *et al.*[6] allowing one to expand the image of very slow particles to effectively fill the available area of the PSD and so fully utilize the available pixel resolution. Consequently, this permits a detailed study of threshold ionization in the meV range.[7] At the opposite extreme, when dealing with energies above 5 eV, the use of VMI so far has been very limited since it would require the use of an expensive large-area PSD and/or high electric fields in order to capture the complete image of a 4π distribution of electrons/ions on the detector. Inversion techniques to recover the

[a)]Currently at: Synchrotron SOLEIL, L'Orme des Merisiers, St Aubin, BP 48, 91192 Gif-sur-Yvette Cedex, France.
[b)]Also at: CEA/DSM/DRECAM/SPAM, Laboratoire Francis Perrin, CNRS URA 2453, Bât 522, CEA Saclay, 91191 Gif-sur-Yvette Cedex, France.
[c)]Author to whom correspondence should be addressed; electronic mail: laurent.nahon@synchrotron-soleil.fr
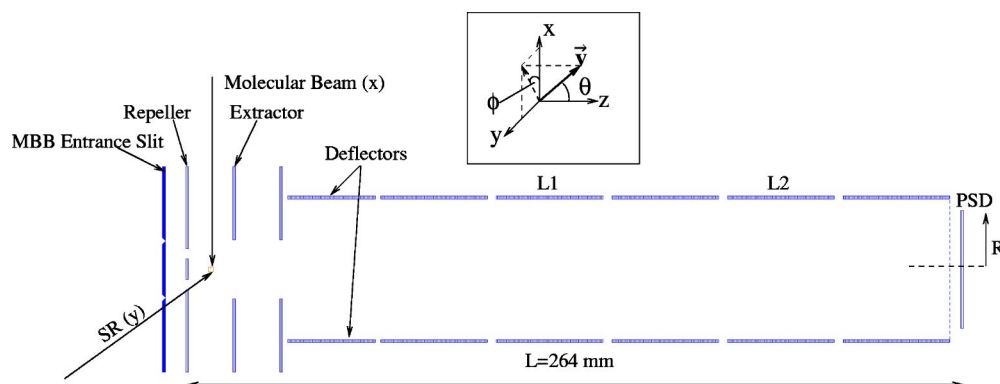
FIG. 1. (Color online) Schematics of the electrostatic structure of the DELICIOUS VMI. The interaction zone is located in the middle of the repeller (potential V_{rep}) and extractor plate (potential V_{ext}), the molecular beam axis coming from the top of the figure (x axis), and the ionizing radiation being perpendicular to the figure plane (y axis). L is the total TOF length and R is the maximum radius of PSD. Also shown is the nonoptimized double Eizel lens focusing system used as a guess for the genetic algorithm (see Sec. III A), as well as the deflector steering plates and the open-ring repeller allowing the collection of electrons towards another electrostatic spectrometer for tandem electron/ion coincidence operation. Only the first electrode corresponding to the entrance slit of the electron analyzer is shown. v is the velocity vector of a particle used in the simulation and its direction is defined by the (θ, ϕ) angles.

complete 3D data from the recorded 2D projection images rely, however, on the inclusion of the full 4π distribution in the projection at the detector.[5]

In this article we present a modified VMI spectrometer design intended for application in molecular photoionization studies on randomly oriented and fixed-in-space molecules. For such studies, synchrotron radiation (SR), with its selectable polarization and easy tunability over tens of eV in the VUV/XUV range, is our preferred source, allowing detailed investigation of single-photon ionization dynamical features. As well as requiring an increase in the upper limit for the energy of the fragment—whether ion or electron—which can be imaged, use with synchrotron sources introduces other constraints. Although modern SR beamlines will produce a small spot size ($\leqslant 250~\mu$m) at the focus, nearly comparable to that achievable with focused laser sources, the effective SR ionization volume can be much more extended in the photon beam propagation direction due to a gentle focusing of the last mirror (more than 1 meter focal length in general), such that there is not a well-defined light beam waist. Even with a skimmed molecular beam source, the molecular beam's divergence will result in it having a width in the interaction region that may be several mm across. The effective ionization volume (formed by the orthogonal geometric intersection of the pencil-like photon- and molecular beams) may thus have an effective length of several mm along the SR beam direction, and may be even worse with an unskimmed or effusive sample source.

This contrasts with a typical laser chemical dynamics experiment employing multiphoton ionization, where a tighter focus might be desired ($f \leqslant 50$ cm). A more pronounced beam waist (or "dog-bone" geometry) is produced in the interaction zone, and the threshold behavior of the nonlinear ionization process can then result in an ionization source whose effective size may be restricted along the light beam direction to a length of the order of $\sim 100~\mu$m, comparable to its transverse dimensions.[8] We will thus require the modified design to meet what are possibly more demanding focusing conditions, taking into account the width of an

extended source discussed in the preceding paragraph, than were demonstrated in the original Eppink and Parker design.

The quasi-cw nature of synchrotron radiation is particularly suited to the performance of electron-ion coincidence experiments in order to get a state-to-state analysis of dissociative ionization processes,[9] to study molecule-frame photoelectron angular distributions (see for instance Refs. 10 and 11), or for more general investigation of electron-ion recoil vector correlations.[12] Such experiments require, however, the collection of particles (say electrons) by, for instance, an electrostatic analyzer mounted in a tandem assembly on the opposite side of the source from the VMI (operated in the ion mode). For this reason our design must also incorporate an appropriate aperture in the repeller electrode fitted to the rear of the VMI spectrometer, to permit oppositely charged particles to be extracted in an opposite direction from the VMI instrument in coincidence mode,[13] without any deterioration in the properties of the VMI instrument when it is required to be operated for either electrons or ions alone in a single, noncoincidence mode.

The imaging of this device maps the transverse velocity components of the charged particle to the radial detector coordinate in a manner intended to be independent of initial location in the source region. The aim is to infer the full 3D velocity distribution via a mathematical deconvolution process. As such, we are not directly interested in the axial velocity component; indeed, most deconvolution procedures require this to be compressed in order to achieve a "flat" 2D projection image.[3] This contrasts with other SR imaging devices which can exploit the interpulse gaps in the few-bunch synchrotron operation mode to record electron time-of-flight, directly measuring the axial velocity.[11] Due, however, to the short duration of these gaps (typically a few hundred ns) this provides limited resolution for all but the slowest electrons. Here, the VMI technique, and associated deconvolutions, can be applied in the more common quasi-cw multibunch SR operation mode, and so its use extends to much higher energies.

Our optimized VMI design has been initially imple-

mented in the newly developed "DELICIOUS" (Dichroism and ELectron/Ion Coincidence in Ionization Using Synchrotron) Angle Resolved PhotoElectron-PhotoIon COincidence (ARPEPICO) system, which is dedicated to molecular photoionization studies on randomly oriented and fixed-in-space molecules. This complete apparatus has been designed to meet our main goal, i.e., the exploration of the radial and angular distributions of photoelectron/photoion during molecular photoionization processes that may involve autoionization, shape resonances, or strong dynamical variation of the asymmetric forward/backward electron emission from the photoionization of randomly oriented chiral species with circularly polarized light (CDAD).[14] These phenomena all fall in a regime extending well above threshold, and so typically require the spectrometer to operate up to some 20 eV above the ionization thresholds.

While meeting the above-identified constraints, the principal feature of our modified design is the presence of a double Einzel lens in the drift tube, allowing us to collect the full, 4π electrons in the kinetic energy range required with a satisfactory resolution, while keeping a reasonable PSD size and moderate electric fields. In the next section we present the overall design of the modified VMI as compared to the Eppink and Parker[4] design, followed in Sec. III by some electrostatic simulations of both the open-slit repeller and of the double-lens focusing system. These simulations will be then compared in Sec. IV with experimental images recorded with the instrument installed in the DELICIOUS system. Finally, in the last section, we will discuss the capabilities of the present spectrometer and the extension of the double-lens system to other VMI geometries.

II. OVERVIEW OF VMI DESIGN

Starting from the initially proposed VMI design of Eppink and Parker,[4] it is *a priori* possible to a get a similar focusing effect and resolution by scaling down or scaling up the whole spectrometer and PSD assembly sizes in order to adapt the VMI to the available experimental chamber and to meet other constraints. The only two important parameters that cannot readily be scaled are the pixel size for a given PSD technology and the size of the source volume, defined by the intersection of the molecular beam and of the light beam. In order to avoid resolution limitations due to these two attributes, it is possible to build up a rather large apparatus, with limitations mostly related to the consequent cost.

On the other hand, in order to optimize the instrument for a given scientific problem and practical circumstance, it is possible also to vary the length-to-radius (L/R) ratio of a VMI spectrometer. For a fixed given PSD size and maximum electric potential on the repeller plate, a smaller L/R ratio will permit a higher maximum kinetic energy (E_{max}) for which a 4π collection efficiency can still be obtained, since E_{max} scales roughly as $(R/L)^2$. But, the squatter spectrometer geometry that then results is detrimental to the achievable kinetic energy resolution and also to the mass resolution in the ion TOF mode of operation of the VMI instrument.

In the present case we had to work to constraints such as the maximum PSD size and vacuum chamber dimensions.

Because of the desired ability to operate a coincidence detection mode, we decided to use a crossed-delay line anode-based PSD (Ref. 15) developed in-house at LURE which has a maximum 40 mm detection diameter. Unlike the more usual choice (for a VMI system) of CCD camera-based PSD system, this technology is capable of precise (sub-ns) time correlation for coincidence detection schemes, as well as high-resolution 2D position determination. Also, the DELICIOUS instrument is housed inside the SAPHIRS molecular beam chamber,[16] imposing geometrical constraints such as a maximum distance between the spectrometer axis and the μ-metal magnetic shielding at the molecular beam skimmer bulkhead of just 40 mm. Note that in these conditions the source volume can be approximated by an elongated cylindrical shape along the y axis (the SR light beam direction) typically 4 mm long, with transverse dimensions (x- and z-axis) on the order of 0.5 mm or less depending on the SR beam cross section.

Taking all these issues into account led us to adopt a 264 mm length L, from the repeller plate to the PSD plane, thus shorter than the initial Eppink and Parker apparatus (367 mm), while keeping the same geometry for the extraction area: 20 mm diameter holes in the extractor and entrance time-of-flight (TOF) plates, spaced by 15 mm. The overall scheme is depicted in Fig. 1.

With such a geometry, a preliminary electrostatic simulation shows that, with a reasonable maximum electric potential of 5 kV on the repeller, the full 4π distribution of particles with a kinetic energy up to 12.7 eV can be collected onto a 40 mm diameter PSD. This idealized value, based on a PSD assumed to be efficient over its whole surface, and a "perfect" simplified spectrometer source region, is insufficient to fulfill our scientific goals. We therefore decided to conceive and build an additional lens system which would allow the full collection of faster electrons (to a minimum of at least 15 eV) with no degradation of the resolution. The optimization of such a lens system will be described in the next section.

Additionally, the source region is required to be coupled in tandem to an electrostatic cylindrical analyzer of the multiplex Bessel box (MBB) type[17] opposing the VMI analyzer, for operating in coincidence mode. Here, this requires that an open annular slit, 3.5 mm wide and with a mean radius of 5.25 mm from the spectrometer axis, be located in the VMI repeller plate. This provides a sufficient free solid angle for particle trajectories to pass from the source to the entrance slits of the MBB, but inevitably may produce some perturbation of the source electrostatic field due to field penetration effects. In the next section we show that this repeller still allows good resolution to be achieved, in accordance with the original Eppink and Parker concept.

Finally, for the sake of versatility we implemented two pairs of deflection electrodes located along the VMI tube allowing one to steer the particle beam in either the gas jet or the SR light beam direction. Such devices are very convenient to make sure of the absolute orientation of the PSD readout coordinates (a necessity for the reliability of CDAD or vector correlation experiments) as well as for possibly correcting the large transverse center-of-mass velocity com-

ponent acquired from the molecular beam inlet, and which might otherwise tend to sweep heavy molecular mass particles, with long flight times towards, or beyond, the edge of the detector.

III. ELECTROSTATIC SIMULATIONS

The performance of our VMI spectrometer in the geometry depicted in Fig. 1 has been examined using code we have developed for electrostatic ray tracing, offering us rather more flexibility than the commonly used SIMION package. A potential gridmap is calculated using a standard successive over-relaxation technique;[18] charged particle trajectories are then numerically integrated across this potential grid using Milne's predictor-corrector method.[19] Large numbers of trajectories can then be followed with a chosen sampling (either random or systematic) of initial conditions (position, velocity, etc.), drawn from appropriate distributions on appropriate boundaries. Due to the cylindrical symmetry of the electric field inside the VMI instrument, the code uses the two-dimensional polar coordinates (r, θ), where $r = \sqrt{y^2 + x^2}$, to describe the particles' trajectories. The outcomes are then analyzed to determine resolution, figures of merit, etc. as a function of the initial conditions.

To be able to know the maximum radial coordinate on the detector (i.e., when the velocity is purely transverse, leading to maximum radial displacement) for a given initial energy of the particle, an energy calibration is required. A suitable calibration curve is given by the expression

$$E = |q|V_{\text{rep}}\frac{R^2}{C^2}, \tag{1}$$

where q is the particle's charge, C is the calibration coefficient, R the radial coordinate at the detector, and V_{rep} the potential on the repeller. For a given instrument configuration we can obtain a calibration coefficient C from fitting Eq. (1) to simulation data obtained by launching trajectories from an ideal, on-axis point source with a fixed polar angle $\theta = 90°$, and systematically increasing energies while recording the final radial coordinate. For the current geometry this gives a value of $C = 39.64$ cm.

All electrodes other than the repeller and extractor are assumed to be grounded unless otherwise stated. It will prove to be convenient to relate many performance properties not to the absolute potential, V_p, applied to a given electrode p, but to its value relative to the repeller electrode potential, V_{rep}. We use the notation $\rho_p \equiv V_p/V_{\text{rep}}$ to indicate such ratios.

The performance of an instrument of given geometry is principally dependent on one such ratio, that of the extraction electrode potential referred to the repeller electrode,[4] $\rho_{\text{ext}} = V_{\text{ext}}/V_{\text{rep}}$. Optimized values, ρ_{ext}(opt.), providing the best focusing are found by a minimization routine that reduces the radial width of the distribution at the detector for a given initial velocity and other conditions. The fully optimized value depends on a number of parameters, the most critical being the geometry of the VMI spectrometer and the ionization volume. For a fixed choice of repeller potential the optimized ρ_{ext} varies slightly (but less than 0.01%) with the
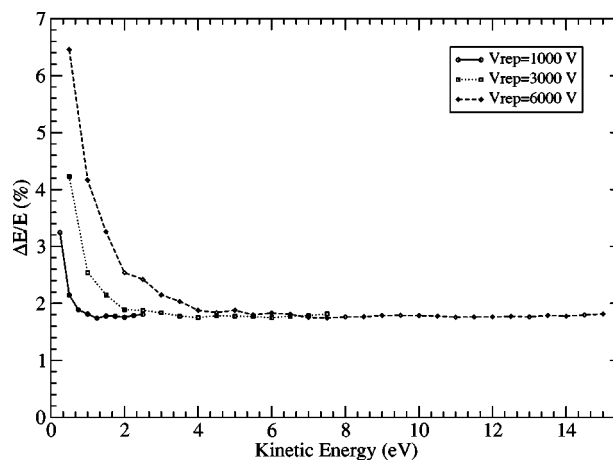

FIG. 2. Energy resolution curves for three different repeller voltages in a configuration with no lenses. Each point of the curves was calculated by launching 1000 random trajectories with a fixed angle $\theta = 90°$ and within a rectangular volume source of dimensions $x, z = 0.5$ and $y = 4$ mm. The resolution is then taken at the FWHM of the peak corresponding to the energy sampled.

kinetic energy of the particle (chromaticity), and with its polar ejection angle, θ, where we have observed a variation of nearly 2% in the 0 to 180° range. Furthermore, ρ_{ext}(opt.) is also a weak function of the repeller voltage itself, presumably as a consequence of external field penetration effects, and we have seen during the simulations a shift of 0.2% in its value when V_{rep} is raised from 1000 to 6000 V. Thus, in order to reduce the complexity of the simulations, we will henceforth consider operation with a single preferred parameter, ρ_{ext}, which is optimized for $\theta = 90°$ and $V_{\text{rep}} = 3000$ V.

Under given conditions, including a specified V_{rep}, the achievable energy resolution dictated by the radial dispersion at the detector varies nonlinearly across the detector surface. To estimate the kinetic energy resolution, $\Delta E/E$, for a given energy and choice of configuration, potentials etc., 1000 random trajectories for a fixed velocity directed perpendicular to the VMI axis ($\theta = 90°$) are followed, with initial coordinates sampled within the finite source volume. Unless otherwise noted, an ionization source volume appropriate to conditions met on a typical SR beamline has been assumed in the electrostatic simulations, with an elongated shape as discussed in Sec. II. The energy resolution is then obtained as the full width at half maximum (FWHM) of the radial distribution at the detector, converted to energy via the calibration determined from Eq. (1). After repeating this routine for a range of energies, the overall results are as depicted in Fig. 2 for three different repeller voltages.

The figure gives an energy resolution, $\Delta E/E$, of 1.8% for particles of 1 eV kinetic energy with $V_{\text{rep}} = 1000$ V. However, Eppink and Parker quote a value of 0.9% in Ref. 4. The difference can be explained mainly by the chosen dimension of the source, which in our case has a 4 mm spread along the SR (y) axis and a discrete value of 500μm along the instrumental (z) axis, while Eppink and Parker assume a 3 mm spread along the y axis and an idealized, infinitely thin source in the z direction. Furthermore, our result is obtained with ρ_{ext} optimized for particles of an energy corresponding to half the maximum pass energy and with $V_{\text{rep}} = 3000$ V,
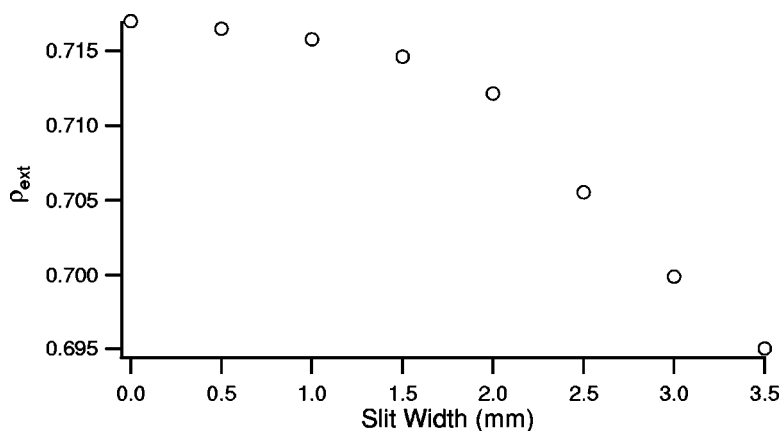
FIG. 3. Variation of the optimum focusing ratio (ρ_{ext}) as a function of the radial width of the open slit in the repeller plate as given by electrostatic simulations in which a simple drift tube has been modeled (no lensing system).

while their simulation assumes a value of ρ_{ext} optimized for the specific energy and V_{rep} in question (1 eV, 1000 V). If we instead use ρ_{ext} optimized for these same conditions and likewise mimic their source dimensions along the z- and y axis we then find essentially the same energy resolution of 0.94%. This confirms that the annular repeller slit, which has a relatively large open area as compared to their smaller 1- or 2 mm diameter hole on the spectrometer axis, is not detrimental to the achievable energy resolution. The only effect of the annular slit is a slight variation of the focusing parameter ρ_{ext}(opt.) with the width of the slit as displayed in Fig. 3. Such a trend is explained by the fact that the repeller loses efficiency due to a weak field curvature near the aperture, and the potential on the extractor has to be lowered to compensate for this effect. The simulated optimum value is found to be $\rho_{ext}=0.695$ for a 3.5 mm slit width, and this is close to our typical experimental ratio of 0.688, obtained by visually optimizing the width at the external borders of the recorded rings, i.e., at $\theta=90°$.

Since the resolution depends on the kinetic energy, in order to compare different electric and geometrical configurations we have chosen to quote the resolutions at $E_{1/2}$, the kinetic energy equal to half the maximum 4π imaging energy, E_{max}. E_{max} can be obtained from Eq. (1) using the determined calibration coefficient by setting $R=R_{max}$, the nominal radius of the detector. For instance, for a voltage of 6000 V on the repeller, and $R_{max}=20$ mm the maximum energy detected is 15.3 eV, as seen in Fig. 2; hence, the resolution for this configuration will be quoted for $E_{1/2}=7.65$ eV kinetic energy. The calculated resolution does not depend on the repeller voltage and was found to be $\Delta E/E_{1/2}=1.8\%$ in all cases. This is of course assuming an ideal spectrometer (perfect mechanical assembly) and detector (no pixel limitation), and is given for a single launch angle $\theta=90°$. We will see in Sec. IV that in practice, and for a continuous θ distribution, the mathematical inversion which has to be performed on the image to recover the central slice of the Newton sphere parallel to the detector, which corresponds to $\theta=90°$, will result in an effective energy resolution degraded by another factor of 2.

A. Lens optimization procedure

As discussed in the previous section, the reason for introducing an electrostatic lens was to allow the full collection

of particles with high kinetic energy. In order to maintain the simplicity of the VMI concept, both mechanically and electrostatically, we have limited the number of lenses to two, which gives a total number of five electrodes and a final grid in the flight tube.

To obtain the best possible geometry for the multilens system, a genetic algorithm has been used in conjunction with the ray-tracing routines mentioned above. The genetic algorithm works by initially creating a random number of geometric configurations of the multilens system, called genes, and then selecting and combining those deemed to be fit to create a better generation. The program also introduces random mutations to avoid a stagnation of the generations.

To calculate the fitness of the genes an equal weight was given to criteria based on *curvature* and spatial *focusing*. The *curvature* represents the ability of the lens system to successfully image higher energy trajectories maintaining the full 4π collection at the detector; *focusing* is linked to the energy resolution and the capability of focusing the momentum of the particle on the same radial coordinate independently of its original position in the interaction region. In contrast to the electrostatic lens devised by Lebech *et al.*,[20] which aims at achieving a correct curvature and focusing while leaving unchanged the temporal distribution in the direction perpendicular to the detector plane (thus preserving time-of-flight capabilities), here we are not restricted by any temporal requirements since the VMI spectrometer attempts to compress the particles' Newton sphere in this direction.

In order to speed up the convergence of the genetic algorithm an initial guess was fed into the program. Since we had no prior knowledge of the optimal configuration, we chose to input a geometry where the five elements of the multilens had the same width, as shown in Fig. 1. Due to the constraints imposed by the geometry of our vacuum chamber and the magnetic shielding, the radius of the multilens elements had to be fixed to 2.4 cm and did not enter the optimization process. In any case, the radius does not go through a minimum since the smaller it is, the better the curvature for a fixed voltage on L_1 and L_2. Therefore, the only parameters that are varied during the optimization are the position and length of the five electrodes. The geometry output of the genetic algorithm is shown in Fig. 4 for $V_{rep}=3000$ V and fixed voltages on the L_1 and L_2 electrodes equal to 1000 V (i.e., $\rho_{L1}=\rho_{L2}=0.33$). The voltages on the electrodes on each
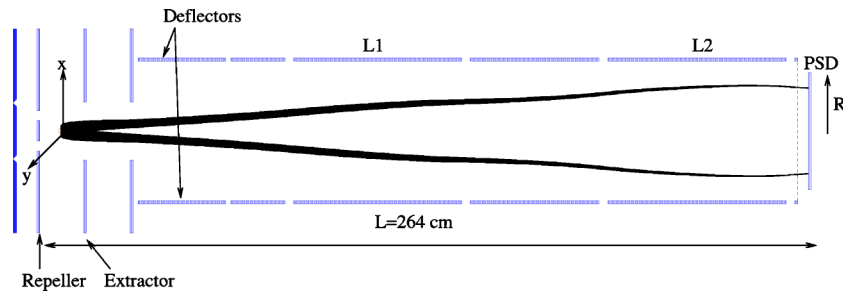
FIG. 4. (Color online) Optimized geometry of the double Einzel lens and the trajectories obtained for $V_{rep}=3000$ V and $V_{L1}=V_{L2}=1000$ V. The curvature and radial focusing were optimized for electrons of 5 eV kinetic energy. Only the position and length of the lens electrodes were allowed to vary. The lengths of the $L1$ and $L2$ electrodes obtained after 44 iterations are 5.6 and 6.1 cm, respectively, while their optimized positions with respect to the source point are 10.85 and 21.8 cm The total length L and radius of the spectrometer remained fixed due to practical geometrical restrictions. The lens geometry shown in Fig. 1 served as the initial guess.

side of the L_1 and L_2 plates were all set to zero. The genes' fitness was calculated for particles with 5 eV kinetic energy and ejection angles of $\theta=90°$. With a first generation of 1000 genes and allowing for 50 random mutations at each generation, the algorithm took 44 iterations to converge to an acceptable level.

To verify the stability of the algorithm we tried different initial guesses but obtained the same final result. Different combinations of voltages ratios, ρ_{L1} and ρ_{L2}, were also fed into the algorithm but, within the range explored ($\Delta\rho_{Li}=\pm0.03$), we observed at most a variation of 8 and 2 mm for the optimized positions of L_1 and L_2, respectively, and less than 1 mm variation on the width of both lenses. It was not deemed necessary to extend the range $\Delta\rho_{Li}$ since, as we will discuss in the next section, there is a limit to the maximum value of ρ_{Li} beyond which the lenses cannot be used, and the best radial focalization is obtained around $\rho_{L1}=\rho_{L2}=0.3$.

B. Ray-tracing simulation of optimized lens performance

We have used the ray-tracing routines to characterize the chosen optimized multilens array (described in Fig. 4) in terms of energy resolution, bandwidth, and calibration curves. This has been summarized in Table I, where the maximum kinetic energy available is shown along with the energy resolution at the half energy, and the energy calibration constant for different electrostatic configurations and for a fixed repeller, $V_{rep}=3000$ V.

By looking at the rows where only one or the other of the two central lens elements has an applied potential, we can examine their independent behavior. Both lenses seem to achieve a similar degree of curvature while keeping a good energy resolution, which in most cases is better than that obtained when operating with no lensing—i.e., 0 V on all lens elements. This implies an additional slight refocusing of the particles as they travel across the electrostatic field produced by the lens. But, once the potential on the lens electrode exceeds $0.3\times V_{rep}$, the energy resolution is degraded. However, some differences between the two lenses have been observed, namely that operation of L_1 has a bigger effect on the optimized focusing ratio ρ_{ext}, which has to be retuned for each set of $[V_{L1}, V_{L2}]$ values. This was somehow expected since the electric fields created at L_1 can more readily penetrate back to the extraction region. Moreover, the

further from the detector are any small deflections induced by the lens fields, the more pronounced these will likely be once propagated to the detector; therefore, the focal plane can be more easily influenced by L_1.

Another difference between the lenses concerns the maximum voltage that can be applied to them (independently) before causing the E- vs R curve to become non-monotonically increasing. If this is occurs, the correlation between the radial coordinate on the detector and the kinetic energy of the particle is no longer unique and the energy distribution cannot then be extracted. For L_2 operating independently, this provides the capability to focus the full 4π distribution for particle trajectories some 0.5 eV higher than can be achieved by L_1 alone.

When both lenses are operated simultaneously the resolution at $E_{1/2}$ can be further improved. From Table I one can

TABLE I. Summary of the performance of the optimized double Einzel lens shown in Fig. 4. The simulation data include the maximum pass energy, energy resolution at $E_{max}/2$, calibration constants (B), and optimized extractor ratios (ρ_{ext}) for different electrostatic configurations. In all cases the repelled was fixed at 3000 V and the resolution was calculated by launching 1000 random trajectories within the specified volume source for a given particle energy equal to $E_{max}/2$.

L_1 (V)	L_2 (V)	ρ_{max}	E_{max} (eV)	B (cm)	$\Delta E/E$ (%)
0	0	0.6951	7.6	NA	1.8
300	0	0.6942	7.9	41.5500	1.7
600	0	0.6935	8.4	30.6014	1.7
900	0	0.6899	9.4	23.1892	1.6
1250	0	0.6774	12.9	16.3547	2.5
300	300	0.6943	8.0	40.2692	1.7
600	300	0.6935	8.6	28.1780	1.7
900	300	0.6897	9.6	22.1674	1.6
300	600	0.6943	8.7	27.7301	1.7
600	600	0.6926	9.0	25.7007	1.7
900	600	0.6895	10.3	20.3891	1.5
300	900	0.6936	9.9	22.1052	1.5
600	900	0.6920	10.4	20.5287	1.5
900	900	0.6881	11.8	17.9955	1.5
0	300	0.6946	7.8	45.7190	1.7
0	600	0.6940	8.4	31.4131	1.7
0	900	0.6940	9.5	23.4427	1.6
0	1300	0.6884	13.4	15.1119	2.0
1000	1000	0.6839	14.0	15.8705	1.9
1100	1100	0.6745	18.9	13.4954	2.6

see that the best configuration in terms of energy resolution and maximum kinetic energy allowed is found for $V_{L1} = V_{L2}$ = 900 V. Beyond that level, the resolution starts to degrade with increasing potentials. The maximum kinetic energy that can be sampled when both lenses are operating at 1100 V is E_{max} = 18.9 eV, but with the consequent loss in the energy resolution. Note that the maximum usable voltages allowed in this dual lens mode are lower than that found for each lens independently.

If the lenses are used, the calibration expression, Eq. (1), can be adapted by introducing at least a cubic term to the polynomial fitting function, giving

$$E = |q| V_{rep} \left(\frac{R^2}{C^2} + \frac{R^3}{B^3} + \cdots \right), \tag{2}$$

where the coefficient C has the same value as that of Eq. (1), and B is constant for a given pair of values of $\rho_{Li} = V_{Li}/V_{rep}$ ($i = 1, 2$). The calculated values of B are presented in Table I for the different electrostatic configurations.

Normally one will only wish to work with a fixed set of ρ_{Li} (for instance, $\rho_{L1} = \rho_{L2} = 0.3$) and hence only a single calibration will be needed. Nevertheless, the following procedure could be used if multiple configurations are required. First, the constant B should be extracted for several values of ρ_{L1} while keeping $\rho_{L2} = 0$, allowing the calculation of B for any value of ρ_{L1} by interpolation of the coefficients a, b, c, and d from the expression

$$B(\rho_{L1}) = a + b\rho_{L1} + c\rho_{L1}^2 + d\rho_{L2}^3. \tag{3}$$

This should be repeated for $B(\rho_{L2})$ while maintaining ρ_{L1} = 0. If we now make the assumption that both lenses are independent, we then can calculate the constant B for whichever combination of ρ_{L1} and ρ_{L2} according to the equivalent lens conjugation law equation

$$\frac{1}{B^3(\rho_{L1} + \rho_{L2})} = \frac{1}{B^3(\rho_{L1})} + \frac{1}{B^3(\rho_{L2})}. \tag{4}$$

The validity of this method has been tested through simulations by calculating the coefficients (a, b, c, d) for each of the lenses and then comparing the interpolated calibration curve with that obtained by direct calibration. The result can be graphically seen in Fig. 5, where we have attempted to predict the calibration curve for the configurations $V_{L1} = V_{L2}$ = 600, 900, and 1100 V for a repeller voltage, V_{rep} = 3000 V. The approximation gives satisfactory results for low voltages but fails to predict the curves when voltages approaching the maximum limit are used. Hence, the errors incurred in this approximation at the half energy are 1.2%, 3.7%, and 7.8% for $V_{L1} = V_{L2}$ = 600, 900, and 1100 V, respectively, which translate into an energy uncertainty of 54, 216, and 740 meV.

For high voltages the agreement deteriorates further toward the border of the detector's active surface. This requires the extension of the fitting polynomial function, Eq. (2), to include higher order terms for an accurate fit to the simulated behavior. But, more restrictively, as the lens fields are increased the two lenses stop being independent due to the greater field penetration, and so our initial approximation is no longer valid. In these cases, it is recommended to perform
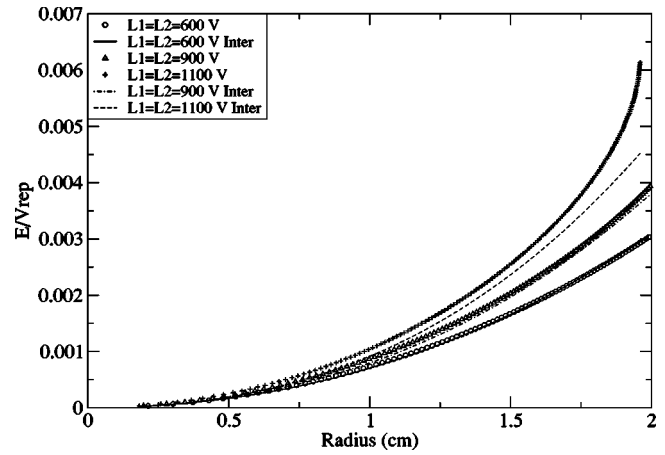

FIG. 5. Energy calibration curves for different electrostatic configurations and V_{rep} = 3000 V. The points represent the simulated values, while the lines correspond to model functions calculated from Eqs. (2)–(4) (see the text for details). The model functions were obtained assuming that the two Einzel lenses are independent of each other. The figure shows that this approximation can be considered valid for $\rho_L = V_L/V_{rep} < = 0.3$.

individual calibrations by fitting simulated data to Eq. (2) extended to include an additional quartic term.

We have simulated the variation of the energy resolution as a function of the particle impact position onto the detector for a number of different electrostatic configurations. The resolution curves obtained are plotted in Fig. 6. By looking at the curves where only one of the lenses is used, we observe that L_2 performs somewhat better at low kinetic energies and at higher energies both lenses behave similarly. For energies beyond ~4.5 eV, Fig. 6(b) shows that the radial focusing given by either lens exceeds that of the spectrometer operated without the lens. If we now look at the combination of both lenses the same trend can be clearly seen, i.e., at high energies the resolution of the multilens configuration is dramatically improved. This trend is even more obvious where both lenses are operated as can be seen in Fig. 6(a), where the energy resolution stays below 0.5% over a several electron volts bandwidth. The resolution curves in the case where $V_{L1} = V_{L2} = 0$ vary less dramatically and reach the ultimate resolution at lower kinetic energies.

It is very interesting to note that the kinetic energy scale in Fig. 6 scales linearly with V_{rep} and V_{Li} voltages. Therefore, for any given particle energy we will always find a multilens electrostatic configuration which gives better resolution than in the case where no lenses are used. This can be easily achieved by lowering the voltage on the repeller and applying an equal voltage on both lenses of around $0.3 \times V_{rep}$. Then, one will be interested in tuning V_{rep} and V_{Li} so that the relevant part of the particles' energy spectrum lies in the large radial region, in order to benefit from the spectacular resolution improvement seen in Fig. 6(a). This approach will of course fail when one wants to detect threshold electrons.

C. Angular resolution

Up to this point we have only referred to the resolution performance in terms of radial resolution (energy). However, another important aspect (seldom mentioned) is the angular resolution, which will have a direct effect on the errors of the
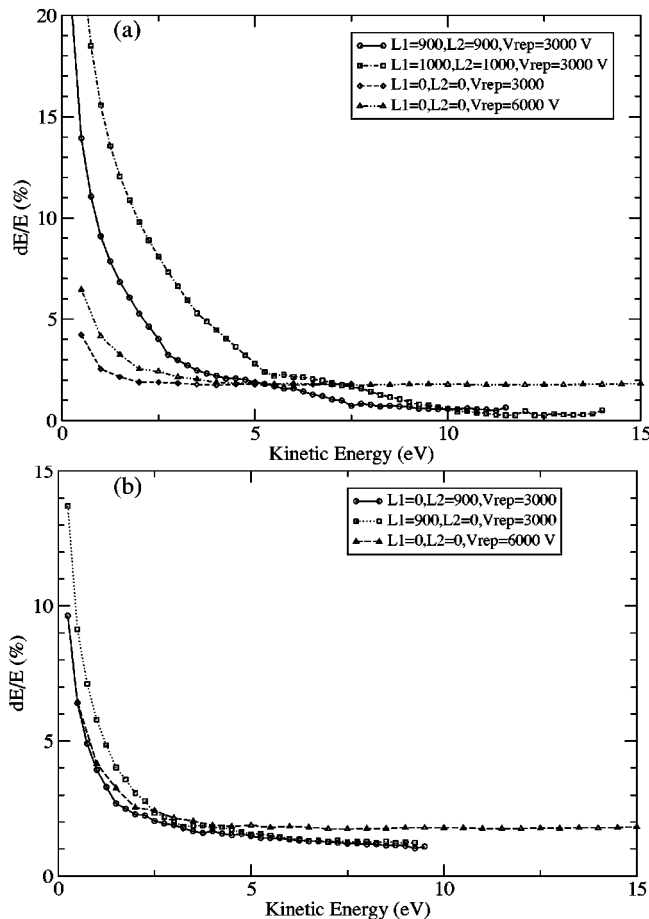
FIG. 6. (a) Simulated energy resolution curves obtained when both lenses are operated simultaneously and with equal voltages. When the lenses are enabled the resolution curves vary more dramatically, becoming worse at low kinetic energies but improving at high energies with respect to the case where lenses are switched off. (b) Simulated energy resolution curves for each independent lens. The behavior of both lenses is very similar, with both curves suggesting a resolution somewhat better at higher energies than that obtained with the lenses disabled.

measured angular parameters that are often of central interest for the process under investigation. This performance is affected by those trajectories which are originated off the instrument axis, with $y_0, x_0 \neq 0$. When a particle is produced off-axis, the plane containing the particle's initial position and the detector axis can rotate around the latter if there is an out-of-plane component of the initial velocity, inducing an rotation of the final azimuthal angle, ϕ_f. Due to the cylindrical symmetry of the electric field inside the spectrometer, the angular momentum around the instrument axis z must be conserved, and the initial angular velocity will vary according to the expression

$$\omega_z = \omega_{z0} \frac{r_0^2}{r^2}, \tag{5}$$

where ω_{z0} and ω_z are the initial and final angular velocities around the z axis, r and r_0 are the initial and final radial coordinates from this axis. Hence, the angular velocity, and consequently the net rotation, will be more pronounced for particles which remain close to the instrument axis. To simulate the deviation from the original azimuthal angle ϕ_0, we have launched random trajectories within our source volume

TABLE II. Mean angular displacement and spread for different E/V_{rep} ratios and two electrostatic configurations—with and without lenses in operation. The presence of the double lens has little effect on the angular distributions.

$E/V_{rep} \times 10^3$	Mean angular displacement (°)	
	$\rho_{L1} = \rho_{L2} = 0$	$\rho_{L1} = \rho_{L2} = 0.3$
0.33	1.4 ± 5.6	1.6 ± 5.7
1.00	0.9 ± 2.0	1.1 ± 3.0
1.67	0.8 ± 2.0	0.9 ± 2.2
2.33	0.8 ± 1.8	0.9 ± 2.1
3.00		0.8 ± 2.1
3.67		0.9 ± 2.0

for different starting assumptions. The results are summarized in Table II. Each row of the table shows the mean and standard deviations after launching 1000 trajectories with random initial velocity and position vectors. The positions fall within a rectangular source of dimensions $x = z = 0.5$, and $y = 4.0$ mm. Since, from Eq. (5), the angular velocity around z varies with the inverse of $r^2 = x^2 + y^2$, faster electrons or ions will tend to travel further from the detector axis, and so will suffer smaller rotation around the axis and a correspondingly lesser angular smearing. Although it is not shown in Table II, this angular deviation will also decrease with the off-axis extent of the source volume, and therefore it is always desirable to have the smallest possible interaction region. From Table II it can also be seen that introducing the two lenses has little effect on the angular resolution.

The angular distributions of the particles in a photodissociation or photoionization process are typically defined by a small set of angular parameters. Most commonly encountered is the asymmetry parameter, β, which occurs in the angular distribution for direct photofragmentation of randomly oriented target species with linearly polarized light within the electric dipole approximation. We have simulated the effect that the angular deviations shown in Table II may have on the value of the derived β parameter by fitting Legendre polynomials to the obtained angular distributions, and we have found that the relative error induced is quite small, ranging from 0.18% of the absolute β value at the highest kinetic energies to 1.25% at the lowest ones. The errors always cause the apparent β value to be smaller in absolute magnitude, due to the smearing out effect of indeterminate rotations away from the initial angle, φ_0.

In another case which is of particular interest to us, direct photoionization of randomly oriented chiral molecules using circularly polarized light,[14,21] the effect that the angular deviation has on the relevant coefficient of a $\cos \theta$ angular term is very small, typically less than 0.1% for all the kinetic energies sampled.

IV. EXPERIMENTAL CAPABILITIES

The DELICIOUS multilens spectrometer has been commissioned recording photoelectron images on two VUV SR beamlines: SU5 (Ref. 22) at LURE (Orsay, France) and POLAR (Ref. 23) at ELETTRA (Trieste, Italy). The spectrometer, with its double-layer μ-metal magnetic shielding,

was placed inside the SAPHIRS molecular beam chamber, where a cold beam of rare gas atoms was intercepted with the SR beam. The polarization vector was set perpendicular to the spectrometer axis, and the typical photon energy bandwidth that we used for the commissioning was in the $1-10$ meV range. During the experiments, the backing pressure was maintained at 1.5 bar, which corresponds to pressures of 2×10^{-4} and 2×10^{-6} mbar in the expansion and ionization chambers, respectively.

The photoelectrons pass through the spectrometer and were detected by a double-multichannel plate stack coupled to a delay-line-based position sensitive detector.[15] Their positions were then coded by a CTNM4 time to digital converter (Institute de Physique Nucleaire, Orsay) and transferred to a computer via a National Instruments acquisition card. Such a detection system has an ultimate spatial resolution of around 50 μm, with maximum sustained and burst counting rates in the 100 kHz and 5 MHz range, respectively. The images were then treated by our recently developed inversion method pBasex[24] to obtain the original radial and angular distributions.

The electron images taken with Xe will exhibit two components corresponding to the $^2P_{3/2}$ and $^2P_{1/2}$ electronic states of Xe^+, with binding energies of 12.13 and 13.44 eV, respectively. The first step of the commissioning is to calculate the constant C of Eq. (1) when no voltage is applied on the lenses. The experimental constant found is $C_{exp}=41.24\pm0.09$ cm, which is close to the simulated value, $C_{sim}=39.64$ cm. However, this small difference means that the maximum energy obtained experimentally is 8% smaller than predicted. The practical difference is further increased by the fact that our detectors seemed to have a smaller effective area of $\phi=36$ mm instead of the nominal 40 mm, all of which restricts our maximum energy to 75% of the expected limit.

Once the C constant has been extracted, we can focus on the energy calibration when only one lens is operated. As suggested in the previous section, we can obtain a third-order polynomial for each individual lens to interpolate the value of B for any ρ_{L1} or ρ_{L2} and then obtain the constant B for any combination of ρ_{L1} and ρ_{L2} using Eq. (4). Figure 7 shows the result when we attempt to guess the experimental calibration curve for $V_{rep}=3000$ V and $V_{L1}=V_{L2}=900$ V by considering L_1 and L_2 to be independent of each other. We can readily see that the agreement is worse than that simulated in Fig. 5, especially at high kinetic energies. The energy error incurred at half the energy is equal to 3.5%, which is also higher than the 1.2% simulated. Therefore, in practice it seems more suitable to perform an independent calibration for each lens combination, which we have included in Fig. 7. Although an independent calibration may seem onerous, note that in practice, since the calibration curves scale linearly with the repeller, the ratios ρ_{L1} and ρ_{L2} will be fixed at 0.3 and only one calibration will be needed. Also plotted in Fig. 7 is the calibration curve obtained with the ray-tracing simulations extracted from Fig. 5. There is a satisfactory closeness between the experimental and theoretical curves, with the latter being shifted 9% towards higher energies.
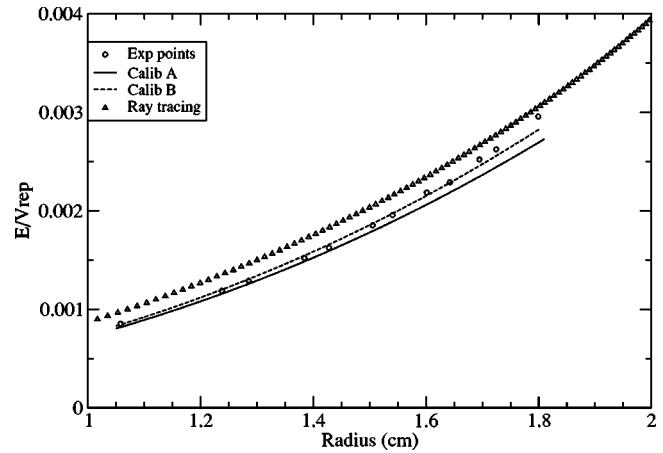
We have investigated the performance of the multilens

FIG. 7. Experimental (circles) and theoretical (triangles) energy calibration curves for $\rho_{L1}=\rho_{L2}=0.3$. The solid and dashed lines represent two types of calibration. Calibration A refers to the one made taking L_1 and L_2 to be independent and using Eq. (4) to obtain the calibration constant. Calibration B was obtained by direct fitting of Eq. (2) to the experimental points shown in this figure. The agreement between A and the experimental points seems to be worse than the one predicted in Fig. 5.

spectrometer in terms of energy resolution. The study is summarized in Table III for a fixed repeller $V_{rep}=3000$ V and different electrostatic configurations. In order to make a fair comparison with theory, we have assumed a detector with a 2 cm radius instead of the experimental 1.8 cm to find the maximum and half energies.

The maximum allowed energies and calibration constants are in close agreement with the ray-tracing results. Concerning the energy resolutions, we see that both lenses independently give the same resolution, which is similar to that obtained with no lenses. However, when both are used simultaneously there is a noticeable improvement on the resolution. This can also be seen in Fig. 8, where the resolution is plotted against the kinetic energy for the configurations shown in Table III. The curve corresponding to both lenses stretches further in energy and the ultimate resolution achieved at E_{max} is 5.5%, in contrast to the 9.2% obtained with no lenses. In practice, we will benefit from this effect by tuning the voltage on the repeller to enlarge the images while keeping $\rho_{L1}=\rho_{L2}=0.3$, to achieve energy resolutions of around 5%–7%. The qualitative behavior of the experimental resolution curves approximates the ones simulated in Fig. 5, but the absolute values differ by a factor of 7. However, the

TABLE III. Summary of the double Einzel lens experimental performance including the calibrations constants, energy resolution at $E_{max}/2$, energy resolution at E_{max}, and maximum kinetic energies for different modes of operation. The best resolution is obtained for $\rho_{L1}=\rho_{L2}=0.3$. The maximum energies shown are given for a 40 mm active area detector and 3000 V on the repeller.

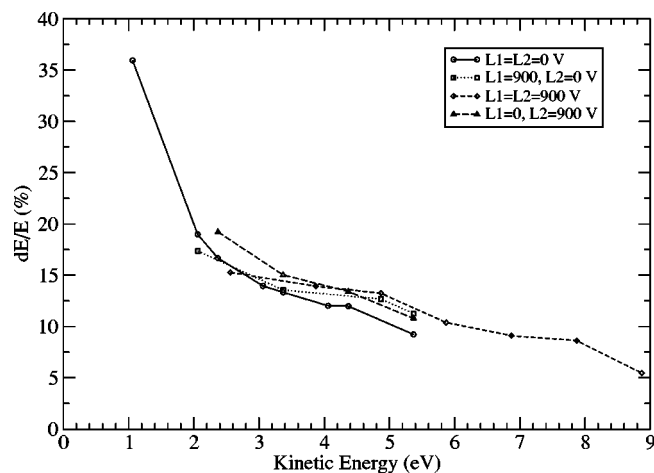| L_1 (V)	L_2 (V)	B (cm)	E_{max} (eV)	$\Delta E/E$ (%)	$\Delta E/E$ (%) @ E_{max}
0	0	NA	7.06	13.0	9.2
0	900	24.72	8.64	13.3	10.8
900	0	24.39	8.71	13.4	11.3
900	900	18.51	10.84	11.7	5.5
1170	990	15.36	13.68	11.5	9.5

FIG. 8. Experimental energy resolution curves extracted from the inverted recorded electron images and corresponding to four different electrostatic configurations for a fixed $V_{rep} = 3000$ V. The ultimate resolution achieved when $\rho_{L1} = \rho_{L2} = 0.3$ is nearly two times better than that obtained with the lenses off.

energy resolutions plotted in Table I are given in the case of an ideal inversion, i.e., at a fixed angle of $\theta = 90°$. If we take into account all the possible angles and the error caused by the mathematical inversion, this factor is reduced to 3.5. This remaining difference could be due to several experimental factors including mechanical misalignments, stray magnetic fields, actual larger volume source, etc., which might result in a degradation of the energy resolution.

Figure 9(a) shows the raw and inverted images of the Xe electrons taken at 23 eV photon energy and with a fixed repeller potential of 5000 V, which is the limit that can be currently applied to the repeller in our spectrometer. The potential on both lenses was set at $\rho_{L1} = \rho_{L2} = 0.3$. The energy resolution can be extracted from the calculated photoelectron spectrum shown in Fig. 9(b) by fitting Gaussians to the observed peaks. The energy resolution found for the $^2P_{3/2}$ state is 6.2%. The angular parameter β can also be extracted from the inversion of the image and was found to be 1.70 and 1.88 for the $^2P_{1/2}$ and $^2P_{3/2}$ states, respectively, in close agreement with the values cited by Holland *et al.*[25] and the theoretical values predicted by Johnson and Cheng,[26] meaning that within our experimental accuracy (± 0.05), no noticeable blurring of the angular distribution is observed.

Experimentally, we recorded Xe photoelectron images up to a photon energy of 26 eV while maintaining the repeller potential at 5 kV. If the lenses were not used, the maximum kinetic energy would be restricted to 9.5 eV. Nevertheless, by making $\rho_{L1} = \rho_{L2} = 0.3$ we are able to detect the $^2P_{3/2}$ electronic state, which has a kinetic energy of 13.87 eV, with a kinetic energy resolution of 6.2%.

V. DISCUSSION

The typical images obtained with the open-slit repeller and the multilens arrangement, such as the one depicted in Fig. 9(a), do not exhibit any noticeable distortion from a circular shape due to the operation of the lenses, such as the coma-like aberration observed by Offerhaus *et al.*,[6] and show a nice fourfold symmetry and a sharp angular resolution with
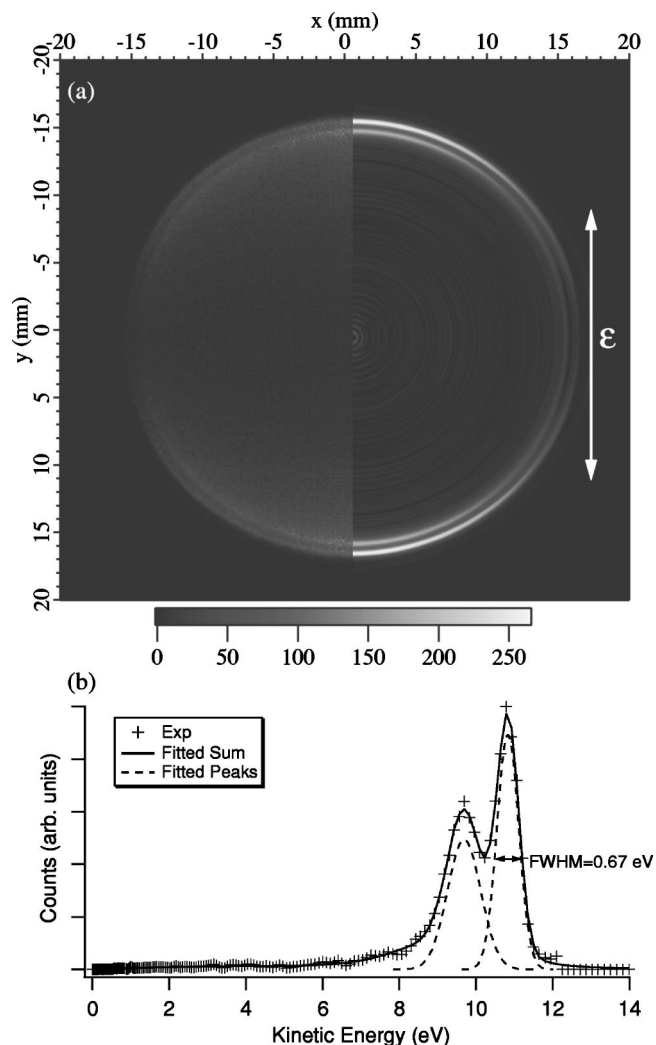

FIG. 9. (a) Raw (left side) and inverted (right side) photoelectron images taken at 23 eV photon energy. The first two electronic states of Xe$^+$ can be clearly appreciated in the inverted image, with the outer ring corresponding to photoelectrons of 10.87 eV. (b) Photoelectron spectrum calculated from the inverted image. The solid line shows the result of a Gaussian multipeak fitting which allows us to estimate the resolution at 6.2% for the $^2P_{3/2}$ state. It can be seen that the photoelectrons are preferentially ejected parallel to the electric vector of the light (ε), corresponding to a positive value of β.

small associated error bars. In fact, we have experimentally confirmed that the energy resolution is very much improved when compared with the no-lens spectrometer, as was predicted by the ray-tracing simulations. This enhancement of the focusing holds true below a given ratio between the voltage on the lens and the repeller of $\rho_{L1} = \rho_{L2} \leqslant 0.3$. Beyond this value the resolution would start to degrade, both in theory and in practice. The achieved energy resolution, although poorer than was found by the simulations, is more than satisfactory for fulfilling our scientific program, mainly dedicated to the study of large molecules with congested electronic bands.

The simulations further demonstrate that a significant improvement in resolution can also be achieved for the case of an ionization source of larger dimensions, for instance, sources likely to be found in experiments using unfocused discharge lamps. Assuming a spherical source of 3 mm diameter, we found a resolution at half the energy of 1.8% for

$\rho_{L1}=\rho_{L2}=0.3$, against 3.3% with the lenses disabled. This amounts to nearly a factor of 2, which will further increase for energies higher than $E_{1/2}$ according to the trend seen in Figs. 6 and 8. By comparing the latter values with those shown in Table I, it can be seen that the lens operation reduces the sensitivity of the spectrometer to the spread of the source volume along the z axis. On the other hand, the source dimension along the y axis has a similar effect on the resolution with or without lenses, and we have observed a factor of 2 degradation when going from a simulated 3 mm to a 6 mm spread along y.

In both the experiments and simulations, the effective energy bandpass is also augmented by a factor of ~1.5 for $\rho_{L1}=\rho_{L2}=0.3$, a number that can be increased to nearly 2.5 by using $\rho_L=0.37$ on both lenses, although at the expense of compromising the energy resolution. If needed, the passband width could be further extended by using commercially available multichannel plate detectors with a 70 mm diameter. In this case one could modify the current geometry of our spectrometer to accommodate this detector while keeping the focal length fixed. If we then switch to high-tension technology we could detect particles up to more than 100 eV for a repeller voltage of 10 kV, while keeping a calculated resolution at half energy equal to 1.2%, better than those shown in Table I. Furthermore, by reducing the focal length by a third, we could reach a maximum energy of 200 eV for $V_{\text{rep}}=10$ kV, at the expense of worsening the resolution by a factor of 1.25, reaching 1.5%. Such a bandpass would now make this type of VMI spectrometer design interesting for a whole range of SR applications in both the valence and core regions where, for instance, the detection of slow photoelectrons and very fast Auger electrons could be done at once and with energy and angular multiplexing. Such a feature could in some cases be quite interesting as compared with the commonly used hemispherical analyzers, which have better resolutions but limited angular and energy multiplex capabilities. The same comments could apply to experiments employing other light sources such as the ones based on high harmonic generation or very high peak power sources like conventional table-top lasers or free electron lasers (FELs), where high kinetic energy particles can be formed in Coulombic explosion processes.[27] For such experiments the VMI spectrometer could then act as an alternative to the magnetic bottle or single TOF commonly used spectrometers, providing a direct energy and angle multiplex detector scheme.

ACKNOWLEDGMENTS

[1] D. W. Chandler and P. L. Houston, J. Chem. Phys. **87**, 1445 (1987).
[2] A. G. Suits and R. E. Continetti, *Imaging in Chemical Dynamics* (American Chemical Society, Washington, D.C., 2000).
[3] C. Bordas, F. Paulig, H. Helm, and D. L. Huestis, Rev. Sci. Instrum. **67**, 2257 (1996).
[4] A. T. J. B. Eppink and D. H. Parker, Rev. Sci. Instrum. **68**, 3477 (1997).
[5] *Imaging in Molecular Dynamics*, edited by B. J. Whitaker (Cambridge University Press, Cambridge, 2003).
[6] H. L. Offerhaus, C. Nicole, F. Lepine, C. Bordas, F. Rosca-Pruna, and M. J. J. Vrakking, Rev. Sci. Instrum. **72**, 3245 (2001).
[7] C. Nicole, H. L. Offerhaus, M. J. J. Vrakking, F. Lepine, and C. Bordas, Phys. Rev. Lett. **88**, 133001 (2002).
[8] S. Speiser and J. Jortner, Chem. Phys. Lett. **44**, 399 (1976).
[9] T. Baer, J. Booze, and K. M. Weitzel, in *Vacuum Ultraviolet Photoionization and Photodissociation of Molecules and Clusters*, edited by C. Y. Ng (World Scientific, Singapore, 1991).
[10] P. Downie and I. Powis, Phys. Rev. Lett. **82**, 2864 (1999).
[11] M. Lebech, J. C. Houver, A. Lafosse, D. Dowek, C. Alcaraz, L. Nahon, and R. R. Lucchese, J. Chem. Phys. **118**, 9653 (2003).
[12] P. Downie and I. Powis, Faraday Discuss. **115**, 103 (2000); A. Lafosse, M. Lebech, J. C. Brenot, P. M. Guyon, O. Jagutzki, L. Spielberger, M. Vervloet, J. C. Houver, and D. Dowek, Phys. Rev. Lett. **84**, 5987 (2000).
[13] M. Takahashi, J. P. Cave, and J. H. D. Eland, Rev. Sci. Instrum. **71**, 1337 (2000).
[14] I. Powis, J. Phys. Chem. A **104**, 878 (2000); J. Chem. Phys. **112**, 301 (2000); M. Stener, G. Fronzoni, D. Di Tommaso, and P. Decleva, *ibid.* **120**, 3284 (2004).
[15] D. Céolin, G. Chaplier, M. Lemonnier, G. A. Garcia, C. Miron, L. Nahon, M. Simon, N. Leclercq, and P. Morin, Rev. Sci. Instrum. **76**, 043302 (2005).
[16] M. Richard-Viard, A. Delboulbe, and M. Vervloet, Chem. Phys. **209**, 159 (1996).
[17] P. Downie, D. J. Reynolds, and I. Powis, Rev. Sci. Instrum. **66**, 3807 (1995).
[18] C. Weber, in *Focusing of Charged Particles*, edited by A. L. Septier (Academic Press, New York, 1967).
[19] W. E. Milne, *Numerical Calculus: Approximations, Interpolation, Finite Differences, Numerical Integration and Curve Fitting* (Princeton University Press, Princeton, NJ, 1949).
[20] M. Lebech, J. C. Houver, and D. Dowek, Rev. Sci. Instrum. **73**, 1866 (2002).
[21] G. A. Garcia, L. Nahon, M. Lebech, J. C. Houver, D. Dowek, and I. Powis, J. Chem. Phys. **119**, 8781 (2003).
[22] L. Nahon, C. Alcaraz, J. L. Marlats, B. Lagarde, F. Polack, R. Thissen, D. Lepère, and K. Ito, Rev. Sci. Instrum. **72**, 1320 (2001); L. Nahon and C. Alcaraz, Appl. Opt. **43**, 1024 (2004).
[23] A. Derossi, F. Lama, M. Piacentini, T. Prosperi, and N. Zema, Rev. Sci. Instrum. **66**, 1718 (1995).
[24] G. A. Garcia, L. Nahon, and I. Powis, Rev. Sci. Instrum. **75**, 4989 (2004).
[25] D. M. P. Holland, A. C. Parr, D. L. Ederer, J. L. Dehmer, and J. B. West, Nucl. Instrum. Methods Phys. Res. **195**, 331 (1982).
[26] W. R. Johnson and K. T. Cheng, Phys. Rev. A **20**, 978 (1979).
[27] H. Wabnitz, L. Bittner, A. R. B. de Castro, R. Dohrmann, P. Gurtler, T. Laarmann, W. Laasch, J. Schulz, A. Swiderski, K. von Haeften, T. Moller, B. Faatz, A. Fateev, J. Feldhaus, C. Gerth, U. Hahn, E. Saldin, E. Schneidmiller, K. Sytchev, K. Tiedtke, R. Treusch, and M. Yurkov, Nature (London) **420**, 482 (2002).